

# An Event-based Algorithm for Simultaneous 6-DOF Camera Pose Tracking and Mapping

Masoud Dayani Najafabadi, Mohammad Reza Ahmadzadeh

**Abstract**—Compared to regular cameras, Dynamic Vision Sensors or Event Cameras can output compact visual data based on a change in the intensity in each pixel location asynchronously. In this paper, we study the application of current image-based SLAM techniques to these novel sensors. To this end, the information in adaptively selected event windows is processed to form motion-compensated images. These images are then used to reconstruct the scene and estimate the 6-DOF pose of the camera. We also propose an inertial version of the event-only pipeline to assess its capabilities. We compare the results of different configurations of the proposed algorithm against the ground truth for sequences of two publicly available event datasets. We also compare the results of the proposed event-inertial pipeline with the state-of-the-art and show it can produce comparable or more accurate results provided the map estimate is reliable.

**Index Terms**—Event-based vision, event camera, KLT tracker, simultaneous localization and mapping (SLAM), state estimation.

## I. INTRODUCTION

In applications such as robot navigation and control, augmented reality, and 3D reconstruction, we need to know a device's location according to a map representation of the environment. Sometimes we are interested in estimating either the map or the robot's pose. Localization or odometry is the problem of estimating the robot's pose when the map is known. On the other hand, the general problem of estimating the device's pose and the scene structure in parallel is called simultaneous localization and mapping (SLAM).

The main challenge in an odometry/SLAM system is to achieve accurate and robust performance in real-time, no matter how severe the conditions are. Certain circumstances, including poor lighting, fast motion, dynamic scene, and long outdoor distances, can adversely complicate the problem. This problem is challenging because the estimation generally requires the optimization of nonlinear equations with a large number of unknown parameters.

One way to address this issue is to use algorithmic techniques and constructs such as parallelization of different parts of the system or the use of efficient data structures [1], [2]. Another approach to achieve acceptable accuracy and robustness against various conditions is to use a range of complementary sensors.

A Dynamic Vision Sensor (DVS) such as [3] is a visual sensor in which each pixel detects the log-intensity change at the pixel location and outputs an *event* independent of the

neighboring pixels. Event cameras are ideal for robotic applications because they allow low latency, high event generation rates, high dynamic range, and low power consumption.

After surveying the related work in Section II, a short review of event data and event generation mechanism is presented in Section III. We then explain different components of the proposed algorithm in Section IV in detail. Section V evaluates the performance of the proposed algorithm. Finally, we conclude our discussion in Section VI.

## II. RELATED WORK

Because our algorithm first represents events as intensity images and then tracks detected features, we review both classical feature-based SLAM and event-based algorithms. Our aim here is to consider only the most relevant work rather than being comprehensive and complete.

PTAM [1] is a feature-based algorithm that separates concepts of localization and mapping and parallelizes both tasks in concurrent threads. This technique not only improves the overall performance but also provides more flexibility; the estimated parameters from one module can be exploited in another without waiting for the process to finish.

ORB-SLAM [2] gradually built on PTAM to address some issues. The last version of this algorithm at the time of this writing, ORB-SLAM3 [4], supports a range of sensors (regular cameras, IMU) with different configurations (monocular, stereo, fisheye, distorted pinhole). This algorithm uses the estimated map to localize pose, supports multi-session mapping, can relocalize when tracking is lost, and reduce the accumulated error with the *loop closing* method. ORB-SLAM performance is limited due to the specifications of regular cameras, despite its robustness and accuracy.

VINS-Mono [5] and its enhanced version, VINS-Fusion [6], are other feature-based methods that fuse different sensors to estimate the pose and structure using a window-based optimization scheme. Unlike ORB-SLAM, which associates features with their descriptors, VINS-Fusion is a KLT-based pipeline. Although it outperforms ORB-SLAM in some situations [4], it still suffers from the same restrictions.

In [7], Gallego et al. surveyed event-based vision and its applications. In the case of event-based odometry and SLAM, researchers have begun by simplifying assumptions for the camera motion or scene structure. For instance, Gallego et al. [8] proposed an algorithm for angular velocity estimation in which only pure 3D rotations were considered. However, most practical applications require more degrees of freedom, and a broader motion model should be considered.

Mueggler et al. [9] proposed a continuous framework for pose estimation based on event data only. The information of every individual event is involved in state estimation. As noted in [10], each event contains little information, so it is better to process a group of events. Additionally, continuous algorithms demand estimating many parameters in a very narrow time window.

In [11], Kim et al. reconstructed intensity images using event data and the features were detected and tracked in these frames. Although the algorithm performs well under fast motion and poor lighting conditions, it needs GPUs for real-time performance.

Rebecq et al. [12] used IMU measurements and events to track 6-DOF camera motion in a window-based optimization framework. They reconstructed motion-compensated images from consecutive overlapped spatiotemporal event windows. Then the features were extracted and tracked using the KLT [13] method. Similarly, Vidal et al. [10] further utilized intensity images. Unlike [12], event windows were synchronized with the timestamp of intensity images. This synchronization can obscure the advantages of asynchronous low-latency event data. Both schemes require IMU measurements to initialize motion parameters and reconstruct frames. They also manually set the event window size for each sequence, which restricts the flexibility of their algorithm.

Similar to our algorithm, the event-based visual-inertial odometry pipeline (EVIO) in [14] adaptively selects the best spatiotemporal event window length based on the events' optical flow. However, while our method, in its basic configuration, depends only on input events and addresses a range of conditions, EVIO relies on IMU readings for state estimation and does not explicitly consider situations where, for example, the camera is motionless.

In this paper, we propose an event-based SLAM algorithm with the following features:

- A novel image reconstruction algorithm adaptively selects the event window size based on camera motion and scene structure and converts them into a motion-compensated image.
- A higher-level KLT-based localization and mapping module exploits map data derived from MC images to estimate the current pose of the camera.
- An event-inertial version of the proposed event-only pipeline is presented to show how additional sensors can improve the algorithm.
- Distorted pinhole and Kannala Brandt [15] camera models are supported, the camera motion has six degrees of freedom (6-DOF), and there is no assumption about the type of scene.
- The proposed algorithm has robust performance in different conditions as long as the map estimate is reliable and there is relative motion between the camera and the scene.

### III. EVENT DATA

If there is a relative motion between the DVS and the scene, the illumination  $I$  at each pixel location changes. When there

is enough change in the log-intensity,  $L(t_k) = \log(I(t_k))$  at current time  $t_k$ , relative to a reference time  $t_r$ , it outputs an event at each pixel coordinate  $\mathbf{x}_k = (x_k, y_k)$ . Formally, if the change in  $L$  is greater than a threshold,  $C$ ,

$$|\Delta L(t_k, t_r)| = |L(t_k) - L(t_r)| > C \quad (1)$$

there is an event

$$\mathbf{e}_k : \{t_k, x_k, y_k, p_k\}$$

where  $p_k$  shows the sign of change, i.e., if  $L(t_k)$  is bigger than  $L(t_r)$ ,  $p_k$  is positive, and it is negative otherwise.

Fig. 1 shows a slice of all events in the sequence `shapes_6dof` from the Public Event Dataset [16]. Each 3D point in the spatiotemporal space in Fig. 1(a) designates an event, color-coded based on event polarities. Each slice of this space represents a spatiotemporal event window.

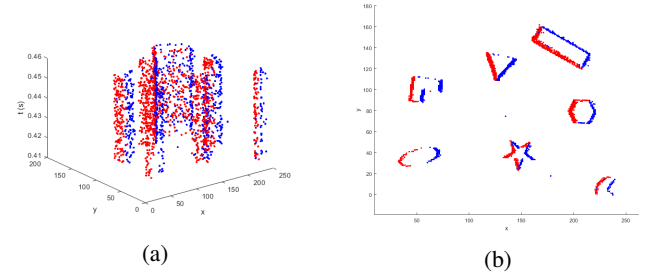


Fig. 1: Representation of a spatiotemporal event window from `shapes_6dof` [16]. (a) Spatiotemporal window of 2000 events starting from a specific timestamp. Blue points show events with positive polarity. (b) 2D view of (a) in the image (x-y) plane.

Since event generation depends on intensity change in each pixel, there is no spatial correlation between adjacent pixels. Each pixel generates events asynchronously as soon as a change in its intensity value is detected. On the other hand, uniform areas in the image cannot contribute to event generation. This redundancy reduction allows lower latencies and faster event generation rates. Events compactly summarize information regarding the scene's high-contrast areas.

Note how the event generation rate depends on the relative motion between the camera and the scene and structure in normal illumination conditions. For a fixed threshold,  $C$ , if the camera traverses slowly through the environment, the event generation rate is low, and event data is noisy. On the other hand, in highly textured scenes, the event generation rate could be high at regular speeds. For specific camera settings, if the camera moves fast in a textured environment, the event generation rate eventually reaches the maximum allowable output bandwidth of the event camera.

We can benefit from available image-based SLAM algorithms by representing event data as a 2D image. To produce the event histogram  $I_r$  for a specific event window  $W_r$  at reference time  $t_r$ , all events in each pixel location are added

$$I_r(\mathbf{x}) = \sum_{\mathbf{e}_k \in W_r} p_k \delta(\mathbf{x} - \mathbf{x}'_k), \quad (2)$$

where  $\delta(\cdot)$  is the continuous Dirac's delta kernel. It is common to replace the continuous delta operator with a discrete-time sampled Gaussian kernel with an arbitrary standard deviation  $\sigma_I$ . The parameter  $p_k$  can be changed based on event polarity or set to constant 1 for all events in the window.

Depending on the camera speed and the length of the event window, the event histograms may suffer from motion distortion. In this case, event coordinates can be corrected before reconstructing these images. The resulting image is called a Motion-Compensated Image or MCI for short.

For a carefully selected event window, we can mitigate the motion distortion using a two-dimensional similarity or rigid body transformation [Sim(2) or SE(2)]. Assuming a constant rotational speed  $\omega$  and translational speed  $\mathbf{v} = (v_x, v_y)$  for each event  $\mathbf{e}_k$  in the window, the warp

$$\begin{bmatrix} x' \\ y' \end{bmatrix} = s \begin{bmatrix} \cos \theta_k & -\sin \theta_k \\ \sin \theta_k & \cos \theta_k \end{bmatrix} \begin{bmatrix} x \\ y \end{bmatrix} + \begin{bmatrix} t_{k,x} \\ t_{k,y} \end{bmatrix} \quad (3)$$

maps the event location  $\mathbf{x}$  at  $t_k$  to  $\mathbf{x}'$  at time  $t_r$  where  $\theta_k = \omega \Delta t$ ,  $\mathbf{t}_k = \mathbf{v} \Delta t$ ,  $s$  is the arbitrary scale, and  $\Delta t = |t_k - t_r|$ . Event coordinates should be normalized based on the camera intrinsics beforehand.

When the relative transform  $T_{t_r, t_k}$  and the depth  $Z(\mathbf{x}_k)$  of each event in the window are known, a SE(3) mapping can be used to warp events:

$$\mathbf{x}'_k = \pi_0(T_{t_r, t_k}[Z(\mathbf{x}_k)\pi_0^{-1}(\mathbf{x}_k)]). \quad (4)$$

Here  $\pi_0(\cdot)$  projects the 3D point to the image plane viewed from the current pose, and  $\pi_0^{-1}(\cdot)$  is its inverse operation. In this case, we first retrieve the 3D feature point associated with each event, seen from the current camera position, and map it to a reference location.

If we extract feature points from the reference reconstructed frame and track them across the current image, it is possible to estimate the parameters of (3) and (4) for all events between these frames. For this, we minimize the reprojection error between each warped reference feature location  $\mathbf{x}_i$  and the corresponding match  $\mathbf{x}_j$  in the current frame using

$$\boldsymbol{\theta}^* = \underset{\boldsymbol{\theta}^*}{\operatorname{argmin.}} \sum_{i,j \in J} \mathbf{e}_{ij}^T(\mathbf{x}) \boldsymbol{\Omega}_{ij} \mathbf{e}_{ij}(\mathbf{x}), \quad (5)$$

where  $\boldsymbol{\theta}^*$  is the transformation parameters,  $\mathbf{e}_{ij} = \mathbf{x}_i - \mathbf{x}_j$ ,  $\boldsymbol{\Omega}_{ij}$  is the information matrix, and  $J$  is the set containing all matched feature pairs between the two frames.

To use the estimated parameters  $\boldsymbol{\theta}^*$  to warp events in the current window, we first convert the relative transform to speed,  $\boldsymbol{\psi}$ , using

$$\boldsymbol{\psi} = \frac{\operatorname{Log}(\boldsymbol{\theta}^*)}{\Delta T},$$

where  $\Delta T$  is the length of the window in units of time and  $\operatorname{Log}(\cdot)$  is the inverse algebra that maps an element of SE(2) or SE(3) to a member of the corresponding tangent space. On the premise that the camera moves slow enough to assume constant speed for all events, the unknown transform between each event location and the reference timestamp,  $T_{t_r, t_k}$ , is

$$T_{t_r, t_k} = \operatorname{Exp}(\boldsymbol{\psi} \Delta t),$$

where  $\Delta t = |t_k - t_r|$  and  $\operatorname{Exp}(\cdot)$  is the exponential map for the corresponding Lie group.

We also distinguish the notion of an image and a frame. While an image is simply a two-dimensional array of numbers, a frame consists of other information, including the timestamp, camera pose, and key points beside the image.

Interested readers can refer to [7] for an in-depth review of the event generation mechanism and event representation.

#### IV. ALGORITHM

Fig. 2 illustrates an overview of the proposed event-based SLAM algorithm. Our pipeline consists of two main components, which run concurrently in separate threads. The first part selects an appropriate spatiotemporal window of input events and reconstructs an image for each event window. The second part of the proposed algorithm extracts features from each input image and tracks them using the KLT method across the following frames. The 6-DOF pose of the camera is then estimated, and the local scene is reconstructed. Sections IV-A and IV-B discuss each component in more detail.

##### A. Event Window Selection and Image Reconstruction

The basic idea of the algorithm is to process events in small chunks and generate an MCI whenever there are enough events. The algorithm uses two sets of event windows to select the appropriate window size and reconstruct the MCI. It continually tracks and accumulates *tiny windows* to determine whether there are enough events. It reconstructs the MCI using the *reconstruction window* consisting of all previously collected events. Fig. 3 illustrates the relationship between the event stream, tiny windows, and reconstruction windows.

This algorithm first selects a spatiotemporal window of input events. Initially, the length of the window,  $N_e$ , is selected arbitrarily and can be adjusted later. At this stage, consecutive event windows have no overlap. The proper event window size depends on the event generation rate. As discussed in Section III, the maximum bandwidth of the event camera limits the event generation rate. For example, in an event camera with a bandwidth of 1 million events per second and a resolution of  $240 \times 180$  pixels, we can expect up to around 23 events per second per pixel. Thus the minimum event generation rate can be chosen based on the bandwidth of the event camera, e.g., one event per pixel per second. We select this threshold solely based on the event camera specifications agnostic to the camera motion and scene.

Based on these observations, the event generation rate is calculated by

$$r = \frac{N_e}{\Delta t W H} \quad (6)$$

where  $\Delta t = t_{e_{N_e}} - t_{e_1}$  is the difference between the first event timestamp,  $t_{e_1}$ , and the last timestamp,  $t_{e_{N_e}}$  in the current window, and  $W$  and  $H$  are the width and height of the event image in pixels, respectively.

If the camera does not move fast enough and the event generation rate is low then the event data will be noisy. The algorithm rejects most tiny windows with an event generation rate less than a threshold,  $th_e$ , and restarts from the initial state.

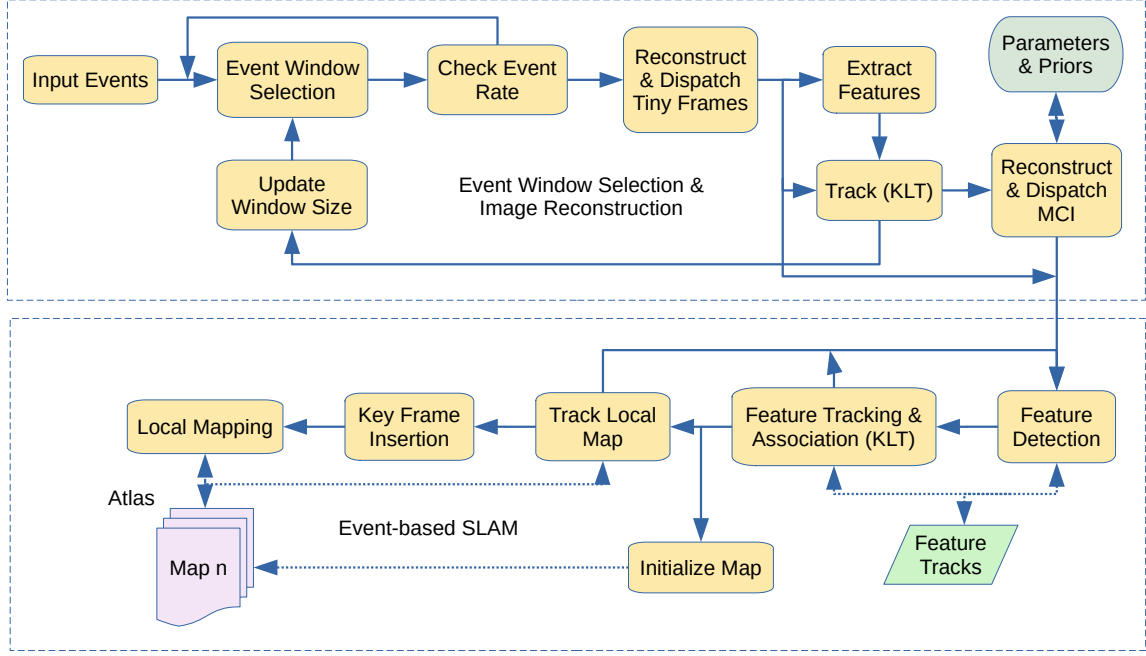


Fig. 2: An overview of the proposed event-based SLAM pipeline.

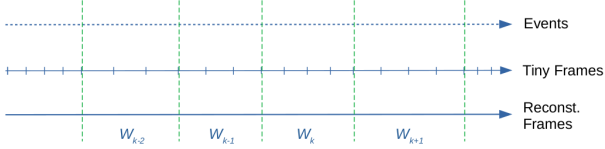


Fig. 3: An illustration of the input event stream, tiny event windows, and non-overlapped reconstruction windows relative to each other.

The only exception is when there are at least  $N_f$  frames. In this case, the algorithm restarts after it generates and dispatches the MCI.

If the event generation rate of the current tiny window is acceptable, a tiny frame is reconstructed based on (2) without motion compensation. The following sections review the main components of the image reconstruction algorithm.

1) *KLT Optical Flow Initialization and Tracking*: In each iteration, the algorithm detects FAST features [17] in the first tiny frame. Since we use image features to determine the displacement in event locations, fewer features are sufficient. If we cannot detect enough features, this step is repeated with the subsequent tiny frames; otherwise, we proceed to the next step.

The algorithm then tracks the reference features in the subsequent frames. We can use the feature matches obtained from the feature tracks for the two-view reconstruction. The map initialization algorithm in [2] is used to estimate the relative pose between the current and the reference frames and the 3D map points corresponding to the feature matches. Due to the small baseline between consecutive frames, most scene reconstruction algorithms cannot yield reliable results. So, we

relieve some of the stringent conditions in [2], i.e., the best model does not have to stand out by a large margin. Because most implementations use the RANSAC method internally, feature matches are still enhanced despite potential failures in scene reconstruction. If a successful reconstruction of the 3D structure is possible, this information is stored and used in the MCI reconstruction algorithm.

We define the median feature displacement metric as the median distance of the tracked image features in pixels. Whenever the median feature displacement in the current tiny frame is higher than a threshold, e.g., five pixels, enough events have been accumulated, and the upcoming MCI reconstruction is commenced.

Note that depending on the type of the scene, the number of detected features varies, but the median feature displacement is not affected. We select the feature displacement threshold based on how much distortion we can tolerate in event locations. This threshold is constant during the operation of the algorithm for all scenes.

After the reconstruction and dispatching of the MCI, the algorithm restarts from the next iteration. Before it begins the next iteration, it updates the size of the tiny windows,  $N_e$ . If  $N_f$  is the number of processed frames and  $N_x$  is the number of expected frames per iteration, the new  $N_e^*$  is

$$N_e^* = \lfloor \frac{N_f N_e}{N_x} \rfloor,$$

where  $\lfloor x \rfloor$  is the greatest integer less than or equal  $x$ .

In this case,  $N_e$  is adjusted according to the camera speed automatically. If the camera speed increases, fewer events satisfy the feature displacement condition, and  $N_e$  decreases. On the other hand, if the camera moves slowly, we need more events for a defined feature displacement, and  $N_e$

increases. Since we did not assume any scene structure,  $N_e$  is independent of the type of the scene.

2) *Motion Compensated Images*: We use different warps to rectify motion distortion in events coordinates and use (2) to reconstruct the MCI. We consider the last event timestamp as the reference and project preceding events in the forward direction.

If there is a reliable 3D reconstruction, we exploit this information in (4) to warp the event locations. As in [10], the median depth of 3D map points is used for all events in the window. Prior to this operation, motion and map parameters can be enhanced using the Bundle Adjustment (BA) method.

On the other hand, if there exists no initial scene and motion estimate, but we have tracked the features across several tiny frames, we can still undistort events using a 2D optimization scheme. In this case, we first fit a Sim(2) or SE(2) motion model to the feature tracks and then reproject events to the reference frame according to (3). We also store this model as initialization parameters for the subsequent iterations.

In some situations, we only know the relative motion estimate. For adequately small motion, we can integrate the IMU measurements to infer the camera motion. If the camera moves slow enough, we can also assume a constant speed and use the motion estimate from the previous iteration. In either case, an average scene depth can be estimated using the 3D motion model of (4) in (5) to minimize the reprojection error.

We run each reconstruction method concurrently in parallel threads. Besides the MC images, we reconstruct the event histogram using (2) with no motion compensation. Finally, we score each image based on its contrast or *sharpness* [18]. To measure image sharpness, we first divide each image into non-overlapped patches and compute the local standard deviation (STD) for each patch. We select and dispatch the image with the highest average local STD. We choose the local STD because it yields more stable results than the global STD.

The KLT algorithm has a poor performance when there is a large baseline between consecutive frames [13]. Although there is not much motion between tiny frames, the distance between the reconstructed frames can be much higher. One way to overcome this issue is to send these frames in addition to MCIs to the event-based tracking algorithm (Section IV-B).

Another approach to ensure smooth transition between consecutive MC frames is to overlap the MC windows. Based on our experiments, this method yields more robust feature tracking in the second level, and hence, it is our preferred method.

### B. Event-based Localization and Mapping

With the MCI from the previous step, the event-based localization module follows an image-based KLT optical flow scheme to estimate the 6-DOF pose of the camera and reconstruct the scene. The basic steps of this algorithm are almost similar to the reconstruction algorithm discussed in Section IV-A.

1) *Initialization*: If there are not enough feature tracks, the algorithm detects new FAST features in the input MCI. It then creates and merges new feature tracks to manage feature

locations across successive images. We use a bucketing grid scheme to ensure a uniform distribution of detected features across images.

The last features are tracked in each subsequent image using the KLT method. If the map is not initialized, we use the two-view reconstruction algorithm between the current and reference frames to reconstruct the scene and recover the camera's relative motion. As in Section IV-A, we use the map initialization algorithm in [2] for this step. After a successful reconstruction, we initialize the map and perform a global bundle adjustment optimization to enhance the estimate.

2) *Tracking The Local Map*: Using feature tracks, we can identify feature associations and the corresponding map points across different frames. Therefore, the current pose of the camera is estimated using an optimization-based framework. To do this, the geometrical distance between the projected map points in the current frame and the corresponding key point observations is minimized.

Due to the camera motion, we might lose track of some features. In this case, the algorithm fails to track features that are not visible in the subsequent frames.

3) *Key Frame Insertion and Local Mapping*: The algorithm inserts a new keyframe whenever there is enough baseline between the current tracked frame and the last keyframe. We use several heuristics to decide when to spawn a new keyframe. Whenever the number of tracked map points falls below a threshold or the median pixel displacement between key points in the current frame and the preceding keyframe is greater than a certain limit, a new keyframe is created.

The local mapping module is very similar to the method used in ORB-SLAM. While our algorithm uses the KLT method to track and associate features, ORB-SLAM detects new matches with descriptors.

In local mapping, we first cull outlier map points based on their rate of observations. Additional map points are then triangulated for the new feature matches between the current and previous keyframes. Finally, a local bundle adjustment optimization enhances the map point estimates.

### C. IMU Measurements

In this section, the necessary changes to incorporate IMU measurements are introduced to show how another sensor module can benefit the proposed algorithm. The preintegration theory and the IMU initialization module of [19] and [2] are used to accomplish this goal. These changes are as follows:

- IMU measurements are integrated between the tiny frames, the reconstruction frames, and the keyframes.
- In the MCI reconstruction module, using the initial pose from the IMU integrations and feature matches, we first find the average depth of the scene in the 3D warp (4) through the optimization framework of (5). We also consider IMU biases and the gravity direction as the state variables in this optimization. The initial gravity direction is evaluated using the first accelerometer reading for the current iteration. These parameters are stored for the subsequent iterations, and the MCI is reconstructed.
- We use an inertial bundle adjustment optimization framework in the MCI generation step with a successfully

reconstructed scene. Besides IMU biases and the gravity direction, we also consider the relative scale.

- We adapt the inertial local bundle adjustment and the mechanism of IMU initialization discussed in [2] in the local mapping algorithm. In summary, the IMU biases, the direction of the gravity, and the relative scale are estimated using an adequate number of keyframes. Such optimization and scale refinement are repeated for several predefined periods.

## V. EXPERIMENTS

To evaluate the performance of the proposed pipeline, we use two publicly available event datasets, the Public Event Dataset [16] and the Multi-vehicle Stereo Event Dataset [20]. The former includes short-duration sequences recorded in different scenes and challenging conditions by a monocular 240×180 pixel DAVIS device. An embedded IMU measures acceleration and angular velocity along three axes of freedom. Most sequences include events, intensity images, IMU measurements, and the ground truth. We only consider the ones for which both the ground truth and IMU measurements are available; hence we exclude sequences from the “depth” group.

Sequences of [20] are recorded with two similar DAVIS 346×260 pixel cameras attached in the stereo configuration. It contains events and intensity images for both cameras, IMU measurements, and the ground truth for the trajectory and depth maps for each frame. We only use the left camera and several representative outdoor sequences, noting that the proposed pipeline is not designed to tackle the stereo case or track longer outdoor distances.

We use several objective criteria to verify the results of the proposed algorithm quantitatively. Since our algorithm generally results in an atlas of multiple disconnected pose graphs, we extend the Relative Pose Error (RPE) in [21] to average the normalized relative errors as

$$\overline{RPE}(\theta) = \frac{1}{|\mathcal{A}|} \sum_{\mathcal{G} \in \mathcal{A}} \frac{1}{D|\mathcal{G}|} \sum_{i,j \in \mathcal{G}} \theta(\mathbf{s}(\Delta T_{i,j}^*) \ominus \Delta T_{i,j}) \quad (7)$$

where  $\mathcal{A}$  is the set of all pose graphs,  $\mathcal{G}$ ,  $\Delta T_{i,j} = T_i \ominus T_j$  is the relative transform between pairs of SE(3) poses in  $\mathcal{G}$ ,  $T_i$  and  $T_j$ ,  $\ominus$  is the inverse of SE(3) Lie algebra,  $D$  is the total traversed distance for the current graph,  $\mathbf{s}()$  is the scaling operation for monocular event-only tracking,  $\theta()$  returns either rotational or translational component of error, and  $*$  indicates the estimate. We normalize RPE by the total traversed distance to reflect the effects of variable length pieces. For the monocular event-only configuration, we calculate the unknown scale by comparing the associated estimate and ground truth pairs and scale the estimate before computing the average error.

Additionally, we consider measures to assess the stability of the pipeline. Total traversed distance or time is the sum of all distances or delta times between consecutive frames in each pose graph.

Before the algorithm processes input events, lens distortions in event pixel locations are rectified using available calibration parameters for each sequence. We choose  $N_x = 3$ , and the initial value of  $N_e$  is 2000 events for sequences of [16] and

6000 for [20]. Since the event frames in [20] have a higher resolution, a higher value for  $N_e$  helps the convergence speed, though starting from 2000 events should eventually converge to the optimal value. Motion-compensated windows have 50% overlap, and Event frames are reconstructed using a Gaussian kernel with  $\sigma_I = 1$  in both tracking levels (tiny frames and MC images). The FAST feature detector threshold is set to a small amount (around zero) because this setting yields the most features and allows us to filter them by their response. We set the KLT tracker with two pyramid levels, a block size of 23×23 pixels, and a maximum bidirectional error of one. These settings are chosen arbitrarily based on our experiments.

Table I summarizes the evaluation results for event-only (E-Only) and event-inertial (E-I-C1) sensor configurations. The stability column of this table is the multiplication of the total traversed distance in meters and time in seconds. Although event-only tracking shows similar or superior results in most cases, the inertial method is more stable. Since more challenging periods can be tracked in the inertial case, the errors grow accordingly. Furthermore, because we do not scale inertial pose graphs, the reported results also include scaling errors.

Besides the challenging conditions of each sequence that can affect the quality of the event image reconstruction and the accuracy of pose estimates, we also note two degrading effects. For lower resolution images of [16], the rays connecting the map points with their respective observations in each frame are so close that the uncertainty in the depth of the subsequent map point estimates grows [22]. Since our pipeline estimates the following poses according to the map, the distance between consecutive poses diminishes, which in turn results in less accurate map estimates. This cycle continues until the tracking is lost. As discussed in [23], this situation can also happen for larger images of [20] recorded by the fisheye camera due to inaccurate translation estimates caused by far map points, especially for outdoor sequences.

Although in the inertial case, the scale information embedded in IMU readings prevents the *shrinking* effect, inaccuracies due to IMU biases can affect map point estimates. If there are not enough map points, the following pose and map point estimates are affected by the growing bias of inertial measurements. In this case, subsequent map point estimates continue to expand after the insertion of each keyframe until the tracking is lost.

The inertial configuration discussed in Table I (E-I-C1) still assumes that the tracking can be lost due to severe conditions, so it tries to reinitialize the map as soon as possible. To further assess the limitations of the proposed algorithm and compare it against the inertial state estimation in [10], we consider two other configurations (E-I-C2 and E-I-C3). We configure our pipeline to enforce continuous tracking without spawning and initializing new maps in unfavorable conditions. In both cases, we disallow the reinitialization of the map and continue to estimate 3D points using inertial readings and feature matches between nearby frames. In the last configuration (E-I-C3), we also fix the tiny event window size to a predefined value and restrict the withdrawal of noisy frames based on the event generation rate. Table II summarizes our preferences for the

TABLE I: Performance evaluation of the proposed algorithm for two event-based configurations compared against the ground truth for some sequences of [16] and [20].

Dataset	Sequence	E-Only			E-I-C1		
		$\overline{RPE}$	$\overline{RPE}$	Stability ( $\times 10^3 m.s$ )	$\overline{RPE}$	$\overline{RPE}$	Stability ( $\times 10^3 m.s$ )
		Position (-)	Rotation (deg/m)		Position (-)	Rotation (deg/m)	
Public Event [16]	shapes_6dof	0.048	0.209	2.31	0.050	0.114	2.50
	shapes_translation	0.084	0.186	2.29	0.092	0.169	2.62
	poster_6dof	0.017	0.062	3.18	0.018	0.057	3.14
	poster_translation	0.005	0.006	2.29	0.005	0.006	2.33
	hdr_poster	0.011	0.025	2.67	0.002	0.007	2.73
	boxes_6dof	0.002	0.004	3.91	0.006	0.008	3.95
	boxes_translation	0.004	0.004	3.40	0.004	0.004	3.46
	hdr_boxes	0.004	0.007	3.08	0.004	0.006	3.07
	dynamic_6dof	0.019	0.041	2.09	0.032	0.117	2.11
Multi- Vehicle Event Stereo [20]	dynamic_translation	0.012	0.018	1.24	0.034	0.032	1.38
	indoor_flying1	0.044	0.041	1.12	0.080	0.046	1.34
	indoor_flying2	0.041	0.032	1.86	0.029	0.019	2.11
	indoor_flying3	0.018	0.006	3.23	0.029	0.008	3.63
	indoor_flying4	0.038	0.013	0.11	0.038	0.016	0.12
	outdoor_day1	0.889	0.033	3.14	1.181	0.041	6.38
	outdoor_night1	0.678	0.003	3.29	1.131	0.008	3.94
	outdoor_night3	1.208	0.009	5.04	1.406	0.017	8.95

TABLE II: Fixed tiny event window size specification for each group of sequences in [16].

Sequence	Number of Events
shapes	2000
dynamic	8000
poster	10000
boxes	12000

length of fixed tiny windows for each group of sequences in [16]. We select these values based on our experience of E-I-C1 with variable window sizes.

Table III compares different inertial configurations using the same RPE metrics of Table I. Both E-I-C2 and E-I-C3 configurations show a significant performance boost to the E-I-C1 configuration. In this case, the prolonged tracking period of E-I-C2 and E-I-C3 configurations provokes more IMU initialization and refinement steps and improves the accuracy of the IMU parameters and the whole system.

The last two columns of Table III also investigate the efficacy of the adaptive selection of the tiny window size. Although the results are similar in most sequences, noting that the window length in E-I-C3 is fixed to the optimal value, a wrongly selected size can impact the performance and accuracy of the system. Therefore, we report the E-I-C2 configuration as our preferred method.

Next, we compare our pipeline against the most relevant algorithm that provides a stable open-source implementation. For this reason, we exclude the methods that utilize the intensity images with the events.

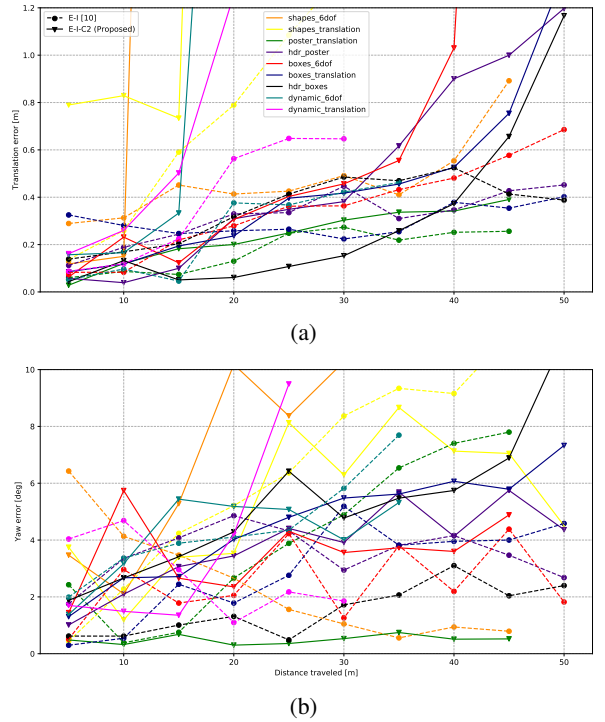


Fig. 4: The comparison between the proposed algorithm and the event-inertial method of [10] in terms of the average relative pose error over a range of distances for the sequences of [16]: (a) average relative translation error, (b) average relative yaw error.

TABLE III: Comparison of the performance of different inertial configurations of the proposed algorithm for sequences of [16].

Sequence	E-I-C1		E-I-C2		E-I-C3	
	$\overline{RPE}$	$\overline{RPE}$	$\overline{RPE}$	$\overline{RPE}$	$\overline{RPE}$	$\overline{RPE}$
	Position ( $\times 10^{-3}$ )	Rotation ( $\times 10^{-3}$ deg/m)	Position ( $\times 10^{-3}$ )	Rotation ( $\times 10^{-3}$ deg/m)	Position ( $\times 10^{-3}$ )	Rotation ( $\times 10^{-3}$ deg/m)
shapes_6dof	50	114	1	6	2	6
shapes_translation	92	169	1	3	1	2
poster_6dof	18	57	1	6	2	7
poster_translation	5	6	4	5	4	5
hdr_poster	2	7	3	7	3	7
boxes_6dof	6	8	1	3	1	2
boxes_translation	4	4	2	4	2	4
hdr_boxes	4	6	2	6	2	6
dynamic_6dof	32	117	2	5	2	5
dynamic_translation	34	32	4	5	4	5

Fig. 4 contrasts the E-I-C2 configuration of the proposed algorithm against the event-inertial method in [10]. We run the latest open-source release of their algorithm<sup>1</sup> for each sequence in [16] using the default configurations (the sequence poster\_6dof is excluded because this implementation of [10] fails to produce reliable results). Similar to [10], we measure and report the average relative translation and yaw error over a range of distances. We calculate the relative pose error between the first one hundred pairs that meet a specific distance range.

Although the window-based state estimator of [10] estimates the pose of the camera and map points simultaneously, our algorithm relies on an accurate map to find the next pose. As a result, any condition that degrades map estimate accuracy will affect our results. For the sequence shapes\_6dof, when the camera moves fast in front of a low-textured poster, the tracking fails due to the lack of detected features, and errors grow exponentially. Even though the scene in sequence dynamic\_6dof is textured, the change in 3D feature locations affects the performance of the proposed method. Despite the poor lighting condition in boxes\_6dof, there are enough reliable map points, and the proposed algorithm outperforms the state-of-the-art based on the translation errors.

Based on our experiments, while the state estimator of [10] can produce more accurate results locally, the proposed algorithm can outperform over longer distances as long as the map estimates are reliable. As mentioned before, when the map estimates are valid, it will affect the subsequent pose estimates even when some map points are no longer visible. Consequently, although the results are not explicitly shown here, we claim that the proposed pipeline can reduce the absolute pose error (APE) when these conditions are met.

Fig. 5 compares the absolute estimated position of the results of Fig. 4 for the sequence boxes\_6dof. We use the APE tools in [2] to align the first 15 seconds of the estimates with the ground truth. In this case, the proposed method can track the ground truth more accurately.

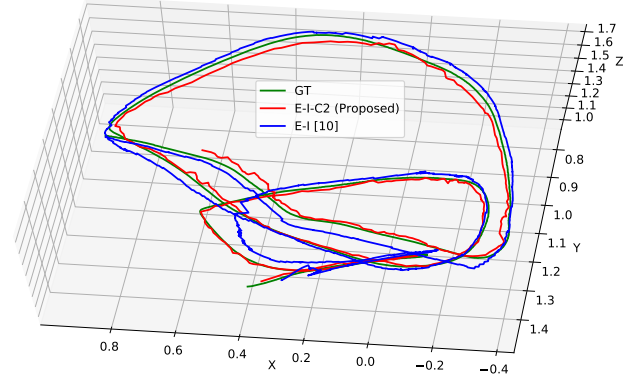


Fig. 5: The absolute estimated positions of the proposed algorithm and the event-inertial method of [10] are compared against the ground truth in terms of the APE for the first 15 seconds of the sequence boxes\_6dof.

Although we have not tried to optimize the performance of the proposed algorithm, we present the average tracking time statistics to contrast the computation cost of each module. In particular, we measure and report the performance of the main tracking thread (MTH), the first-level event image reconstruction module (L1), and the second-level event frame tracking thread (L2). Since it almost takes several tiny frames in L1 and one iteration of L2 for the main tracking thread to process input events, we include the timing as per motion-compensated frames (MCF) and as per tiny frame (TF). Assuming there are three TF for each MCF on average, we subtract double L1 values from the MCF results and report the per TF results. The timing statistics for the local mapping thread are not reported here. We run our pipeline on a system with an Intel Core-i7 9700K CPU, 64 GB RAM, and Ubuntu 20.04 LTS operating system.

Table IV summarizes the timing results of different components of our pipeline for two sensor configurations and some

<sup>1</sup>[https://github.com/uzh-rpg/rpg\\_ultimate\\_slam\\_open](https://github.com/uzh-rpg/rpg_ultimate_slam_open)

TABLE IV: Average tracking time statistics in milliseconds for three main modules of the proposed algorithm, calculated for representative sequences of [16] and [20].

Sequence	Event-Only				Event-Inertial-C1			
	MTH	MTH	L1	L2	MTH	MTH	L1	L2
	/MCF	/TF	/TF	/TF	/MCF	/TF	/TF	/TF
shapes_6dof	72	48	12	6	82	56	13	7
poster_6dof	158	106	26	7	173	119	27	9
boxes_6dof	158	106	26	7	174	118	28	9
dynamic_6dof	138	92	23	7	157	107	25	9
indoor_flying1	139	93	23	8	147	99	24	15
outdoor_day1	171	115	28	5	185	127	29	10
outdoor_night1	187	125	31	5	202	138	32	14

representative sequences of both datasets [16] and [20]. The overall performance of our algorithm is several times lower than the real-time. Note that more textured sequences demand more processing power. The addition of the IMU slightly increases the performance cost of our method. Based on these results, the reconstruction of each MCF is generally the most costly operation. It takes about the same amount of time to reconstruct an MCF, around 28 ms on average, consistent across all configurations and datasets. The timing results of L2 are only comparable across the Public Event dataset. For sequences of [20], the cost of the inertial L2 module is almost twice the performance of the event-only case. One reason for this difference could be the high depth variation inherent in the fisheye camera and the difficulty of scale estimation and refinement involved in inertial tracking in this case (although the local mapping is performed in a separate thread, the inertial L2 must wait because of the map change).

## VI. CONCLUSION

We proposed an algorithm that reconstructs MC images from the adaptively selected event windows and uses the event images to estimate the structure and trajectory. The first module tracks FAST features across multiple event histograms to choose the best event window size and resolve the parameters needed for MCI generation. After reconstruction, it sends the best MCI representation to an image-based SLAM to initialize the map and track the 6-DOF pose of the camera in it. Furthermore, we showed how to utilize inertial measurements to improve the performance of the event-only algorithm.

We compared the estimated trajectory of different configurations of the proposed pipeline with the ground truth for sequences of two publicly available event datasets. Although the algorithm produces accurate results in most cases, its performance depends on the reliability of the map estimate. We also showed that the proposed algorithm outperforms the state-of-the-art as long as a valid map estimate is available.

Although the event window selection module is costly, it can still be used in most event-based algorithms to select the best event window without reconstructing the MCI. It is possible to use different techniques such as relocalization or loop-closing to improve the accuracy of the map, the overall performance, and the algorithm's stability. These techniques

generally extract and use descriptors to link different segments of a pose graph. One can consider event-based descriptors for that purpose or extract descriptors from regular intensity images, which are processed along with the event stream.

## REFERENCES

- [1] G. Klein and D. Murray, "Parallel tracking and mapping for small ar workspaces," in *2007 6th IEEE and ACM International Symposium on Mixed and Augmented Reality*, pp. 225–234, 2007.
- [2] R. Mur-Artal, J. M. M. Montiel, and J. D. Tardos, "ORB-SLAM: A versatile and accurate monocular SLAM system," *IEEE Transactions on Robotics*, vol. 31, no. 5, p. 1147–1163, 2015.
- [3] P. Lichtsteiner, C. Posch, and T. Delbruck, "A  $128 \times 128$  120 db 15  $\mu$ s latency asynchronous temporal contrast vision sensor," *IEEE Journal of Solid-State Circuits*, vol. 43, no. 2, pp. 566–576, 2008.
- [4] C. Campos, R. Elvira, J. J. G. Rodríguez, J. M. M. Montiel, and J. D. Tardós, "ORB-SLAM3: An accurate open-source library for visual, visual-inertial, and multimap SLAM," *IEEE Transactions on Robotics*, vol. 37, no. 6, pp. 1874–1890, 2021.
- [5] T. Qin, P. Li, and S. Shen, "VINS-Mono: A robust and versatile monocular visual-inertial state estimator," *IEEE Transactions on Robotics*, vol. 34, no. 4, pp. 1004–1020, 2018.
- [6] T. Qin, J. Pan, S. Cao, and S. Shen, "A general optimization-based framework for local odometry estimation with multiple sensors," 2019.
- [7] G. Gallego, T. Delbrück, G. Orchard, C. Bartolozzi, B. Taba, A. Censi, S. Leutenegger, A. J. Davison, J. Conradt, K. Daniilidis, and D. Scaramuzza, "Event-based vision: A survey," *IEEE Transactions on Pattern Analysis and Machine Intelligence*, vol. 44, no. 1, pp. 154–180, 2022.
- [8] G. Gallego and D. Scaramuzza, "Accurate angular velocity estimation with an event camera," *IEEE Robotics and Automation Letters*, vol. 2, no. 2, pp. 632–639, 2017.
- [9] E. Mueggler, G. Gallego, and D. Scaramuzza, "Continuous-time trajectory estimation for event-based vision sensors," in *Robotics: Science and Systems*, 2015.
- [10] A. R. Vidal, H. Rebecq, T. Horstschaefer, and D. Scaramuzza, "Ultimate SLAM? combining events, images, and IMU for robust visual SLAM in HDR and high-speed scenarios," *IEEE Robotics and Automation Letters*, vol. 3, no. 2, pp. 994–1001, 2018.
- [11] H. Kim, A. Handa, R. Benosman, S.-H. Ieng, and A. Davison, "Simultaneous mosaicing and tracking with an event camera," in *Proceedings of the British Machine Vision Conference*, BMVA Press, 2014.
- [12] T. H. Henri Rebecq and D. Scaramuzza, "Real-time visual-inertial odometry for event cameras using keyframe-based nonlinear optimization," in *Proceedings of the British Machine Vision Conference (BMVC)* (G. B. Tae-Kyun Kim, Stefanos Zafeiriou and K. Mikolajczyk, eds.), pp. 16.1–16.12, BMVA Press, September 2017.
- [13] B. D. Lucas and T. Kanade, "An iterative image registration technique with an application to stereo vision," in *Proceedings of the 7th International Joint Conference on Artificial Intelligence*, vol. 2 of *IJCAI'81*, p. 674–679, Morgan Kaufmann Publishers Inc., 1981.
- [14] A. Z. Zhu, N. Atanasov, and K. Daniilidis, "Event-based visual inertial odometry," in *2017 IEEE Conference on Computer Vision and Pattern Recognition (CVPR)*, pp. 5816–5824, 2017.

- [15] J. Kannala and S. Brandt, "A generic camera model and calibration method for conventional, wide-angle, and fish-eye lenses," *IEEE Transactions on Pattern Analysis and Machine Intelligence*, vol. 28, no. 8, pp. 1335–1340, 2006.
- [16] E. Mueggler, H. Rebecq, G. Gallego, T. Delbruck, and D. Scaramuzza, "The event-camera dataset and simulator: Event-based data for pose estimation, visual odometry, and SLAM," *The International Journal of Robotics Research*, vol. 36, no. 2, p. 142–149, 2017.
- [17] P. Wyatt and H. Nakai, "Fast feature extraction using approximations to derivatives with summed-area images," in *Proceedings of the 7th Asian Conference on Computer Vision - Volume Part I*, ACCV'06, (Berlin, Heidelberg), p. 776–786, Springer-Verlag, 2006.
- [18] G. Gallego, H. Rebecq, and D. Scaramuzza, "A unifying contrast maximization framework for event cameras, with applications to motion, depth, and optical flow estimation," *2018 IEEE/CVF Conference on Computer Vision and Pattern Recognition*, Jun 2018.
- [19] C. Forster, L. Carlone, F. Dellaert, and D. Scaramuzza, "On-manifold preintegration for real-time visual-inertial odometry," *IEEE Transactions on Robotics*, vol. 33, no. 1, p. 1–21, 2017.
- [20] A. Z. Zhu, D. Thakur, T. Ozaslan, B. Pfrommer, V. Kumar, and K. Daniilidis, "The multivehicle stereo event camera dataset: An event camera dataset for 3D perception," *IEEE Robotics and Automation Letters*, vol. 3, no. 3, p. 2032–2039, 2018.
- [21] J. Sturm, N. Engelhard, F. Endres, W. Burgard, and D. Cremers, "A benchmark for the evaluation of RGB-D SLAM Systems," in *Proc. of the International Conference on Intelligent Robot Systems (IROS)*, Oct. 2012.
- [22] R. H. A. Zisserman, *Multiple View Geometry in Computer Vision*, 2nd Edition. 2 ed., 2004.
- [23] R. Mur-Artal and J. D. Tardós, "ORB-SLAM2: an open-source SLAM system for monocular, stereo and RGB-D cameras," *IEEE Transactions on Robotics*, vol. 33, no. 5, pp. 1255–1262, 2017.
- [24] A. Geiger, P. Lenz, and R. Urtasun, "Are we ready for autonomous driving? the KITTI vision benchmark suite," in *Conference on Computer Vision and Pattern Recognition (CVPR)*, 2012.